Nanoscale

PAPER

View Article Online
View Journal | View Issue

Cite this: *Nanoscale*, 2020, **12**, 3827

Broadband chiral hybrid plasmon modes on nanofingernail substrates†

Paulina Librizzi,[a] Aneek Biswas,[b,c] Roger Chang,[a] Xiang-Tian Kong,[d] Matthew Moocarme,[b,c] Gaurav Ahuja,[d] Ilona Kretzschmar *[a] and Luat T. Vuong *[b,c,d]

Received 27th August 2019,
Accepted 21st January 2020

DOI: 10.1039/c9nr07394a

rsc.li/nanoscale

There is significant interest in the utility of asymmetric nanoaperture arrays as substrates for the surface-enhanced detection, fluorescence, and imaging of individual molecules. This work introduces obliquely-cut, out-of-plane, coaxial layered structures on an aperture edge. We refer to these structures as nanofingernails, which emphasizes their curved, oblique, and out-of-plane features. Broadband coupling into chiral hybrid plasmon modes and helicity-dependent near-field scattering without circular dichroism are demonstrated. The unusually-broadband, multipolar modes of nanofingernail micropore structures exhibit phase retardation effects that may be useful for achieving spatial overlap at different frequencies. The nanofingernail geometry shows new potential for simultaneous polarization-enhanced hyperspectral imaging on apertured, plasmonic surfaces.

Introduction

When light illuminates a sub-wavelength-sized metal structure, absorption and the concomitant excitation of surface charge oscillations or plasmons enhance interactions with the molecules close to the metal.[1–3] Metal films with nanoapertures and micropores may further leverage the enhanced interaction with the molecules.[4–6] Moreover the surface plasmon response of the aperture may be leveraged in other novel ways, for example: to increase imaging resolution;[7–9] to optically and selectively trap particles or molecules at the surface;[10–12] and to monitor flow in optofluidic applications.[13–15] Metal nanoaperture substrates are used in real-world applications for molecular detection and sensing; however, there is a tradeoff between the detection enhancement and substrate fabrication costs. On one hand, 3D nano-sized substrate geometries with non-radial symmetry are desirable for achieving control of the complex near-field polarization patterns, which better probe and sense molecules.[3,16–18] At the same time, it remains a challenge to rapidly and inexpensively fabricate intricately-designed apertured nanostructures over large areas.

In the fabrication of 3D hybrid aperture structures over large areas, angled deposition processes are valuable and chiral nanomaterials are a topic of active interest.[16–19] An intrinsically-chiral structure cannot be superimposed with its mirror image while an extrinsically-chiral structure exhibits mirror symmetry but is not radially-symmetric. In a recent demonstration of the importance of understanding this symmetry, extrinsic chirality is achieved by tilting and illuminating a round, planar structure at oblique incidence; this tilted aperture geometry leads to enhanced light interactions and increased detection sensitivity.[20] Nanocrescents[21] and similar 2D antenna geometries have been incorporated into the design of metamaterials and imaging applications.[17–19] The angled deposition may also be extended to produce structures with intrinsic chirality by varying the angle of deposition with sequential layers.[22,23]

Here, out-of-plane extrinsically-chiral structures around apertures are fabricated by inverted glancing-angle deposition, which combines templating and glancing-angle vapor deposition. The resulting nanofingernails outline the edge of an aperture and protrude from a metal film when the template is removed. The advantage of this process is that shallow, closely-spaced, out-of-plane structures are produced with lateral dimensions on the order of tens of nanometers and the angle of the in-plane broadband light scattering is controllable. Although the structures themselves are extrinsically-chiral,

[a]*Department of Chemical Engineering, City College of New York of the City University of New York (CUNY), New York, New York 10031, USA. E-mail: kretzschmar@ccny.cuny.edu*
[b]*Department of Physics, Graduate Center of the City University of New York (CUNY), New York, New York 10016, USA. E-mail: luatv@ucr.edu*
[c]*Department of Physics, Queens College of the City University of New York (CUNY), Queens, New York 11367, USA*
[d]*Department of Mechanical Engineering, Bourns Hall, University of California at Riverside, Riverside, California 92521, USA*

†Electronic supplementary information (ESI) available: Additional information on nanofingernail thickness and density is provided along with CD measurements, computational details of magnetic fields, angular momentum dynamics, and multipolar modes. See DOI: 10.1039/C9NR07394A

when tilted, the structures exhibit an intrinsically-chiral symmetry.

When illuminated with circularly-polarized light at normal incidence, the scattered near-fields interfere to produce spiralling hot spots around the nanofingernail. These chiral patterns are a manifestation of the near-field intrinsic chirality that is achievable with extrinsically-chiral out-of-plane nanostructures. We also refer to these polarization-dependent spiral patterns as chiral hybrid modes,[24,25] a superposition of longitudinal and transverse multipolar plasmon resonances. The longitudinal modes represent oscillations along the height of the nanofingernail, while transverse plasmon resonances represent oscillations around and in the plane of the micropore. The transverse resonances are multipolar because the micropore is several times larger than wavelengths in the visible spectral range of interest. We emphasize that this chiral scattering occurs in the absence of circular dichroism (either measured or expected) in the far-field. Accompanying chiral hybrid modes are tilted Poynting vector power flows and shifts in the locations of hotspots that depend on circular-polarization handedness.

This Letter aims to demonstrate the unique nanofingernail structure, to illustrate its chiral and multipole plasmon excitation, and to motivate further studies of its geometry. Understanding the angular, polarization-dependent power flows and enhanced intensity profiles associated with asymmetric geometries is nontrivial and therefore described here.

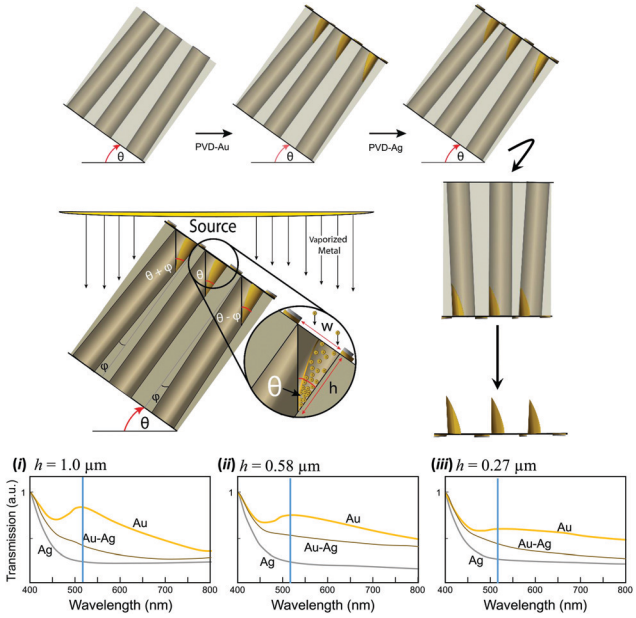

Fig. 1 Schematics of the inverted glancing-angle deposition (I-GLAD) process. Metal atoms are ejected from the PVD source and condense on the pore walls (dark gray columns). The pore walls are etched through the polycarbonate template (light gray). Multiple layers may be deposited. When the polycarbonate is removed, a free-standing array of nanofingernails, or obliquely-cut, extrinsically chiral, out-of-plane nanofingernail results. The regularity of the array orientation is largely limited by the uniformity of the polycarbonate template. Insets: Far-field transmission spectra for all-silver (Ag, grey), all-gold (Au, yellow), and composite (Au–Ag, brown) nanofingernails. As structure height (h) decreases from (i) 1.0 μm, (ii) 0.58 μm, to (iii) 0.27 μm, the broad shoulder emerges red-shifted from the wavelength 530 nm (light-blue line).

Nanofabrication and characterization

The nanofingernails demonstrated in this Letter are produced by sequential physical vapor deposition (PVD) of a gold film followed by a silver film onto a track-etched hard template resulting in bimetallic nanofingernails. The templates are track-etched polycarbonate membrane filters purchased from SPI Supplies (West Chester, PA). The filters are 6 μm thick with pores of 1 μm nominal diameter.

Physical Vapor Deposition (PVD) is performed using a Cressington Desktop HV Pump Station 308R-EM and Cressington Evaporation Supply LT750 for thermal evaporation of the metals. A Cressington Thickness Monitor MTM-10 is used to control the thickness of deposited gold at 75 nm and the thickness of silver at 50 nm with a 0.1 nm reading accuracy. The deposition angle is varied from the horizontal by placing the polycarbonate templates on a platform with an adjustable base. Depositions are carried out at angles of 30°, 45°, 60° and 75°. After the gold and silver vapor deposition, the metal coated polycarbonate templates are placed with the metallic film side facing down onto Kapton tape for SEM analysis (Zeiss EVO 40). The templates are then repeatedly washed with copious amounts of chloroform over a period of 2 hours to dissolve the polycarbonate and expose the nanofingernails.

A schematic representation of the resultant film at each step of the process is shown in Fig. 1. We refer to this process as inverted glazing angle deposition (I-GLAD), which is facile and allows for tuning of both nanofingernail height and thickness. Additionally, the process easily accommodates other materials that are accessible through physical vapor deposition. The pore walls of the track-etched polycarbonate (TEPC) template serve as a substrate where metal vapor condenses. Metal atoms deposit on the inside of the track and result in out-of-plane, obliquely-cut, coaxial nanostructures on the edge of each opening to the track. The vertical alignment of the nanofingernails varies with deposition direction, as shown in the SEM images [Fig. 2].

The height h is delimited by the point at which the upwardly facing lower pore wall intersects with a vertical line drawn from the upper edge of the pore. Physically, this is the point at which the pore wall is no longer in line-of-sight with the source, *i.e.*, metal atoms no longer enter the pore because they are blocked by the pore's upper edge. Second, since metal atoms only condense on the upwardly facing surfaces of the pore walls, the width w of the nanofingernail base, when the structure is viewed in profile, is equal to the pore radius.

The simplicity of this hybrid geometry allows for multiple-metal coaxial geometries. It is worth mentioning some challenges with the most common fabrication techniques of Au–Ag hybrid nanostructures, as reported in a recent review by Cortie *et al.*[26] Seed-mediated growth, galvanic replacement, co-

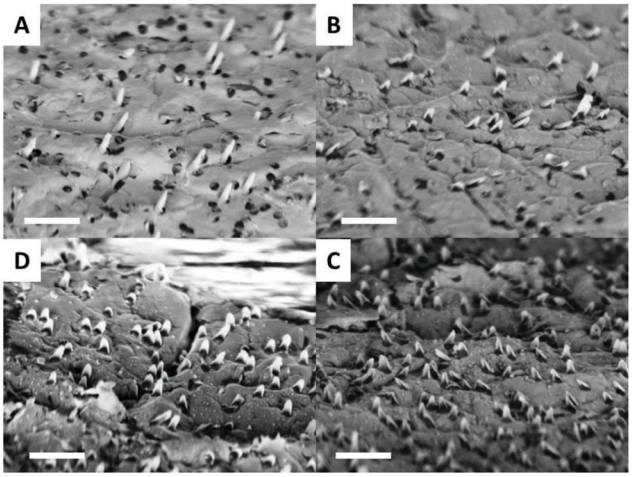

Fig. 2 SEM images of Au–Ag nanofingernails. Fabrication is performed at different deposition angles. Clockwise from top left, (A–D) correspond to deposition angles of 30°, 45°, 60° and 75°, respectively. The scale bars are 5 μm.

precipitation, templated growth and electron beam lithography are methods that are time consuming, involve several fabrication steps or do not reliably produce distinctly hybrid—as opposed to amalgamated—nanostructures. Here, we have fabricated Au–Ag nanofingernails that protrude from an Au–Ag thin film when the polymer template is dissolved in a chloroform rinse. The silver-facing and gold-facing sides of the nanofingernail are opposite to each other, and scatter or absorb in different directions within the plane of the substrate.

In addition, unlike conventional glancing-angled deposition where the minimal height h is limited by shadowing of adjacent structures, the accessible values of the I-GLAD deposition angles θ range from 0° to 90°, where the endpoints of θ = 0° and θ = 90° position the template parallel and perpendicular to the source, respectively. The nanofingernail height $h = w/\tan(\theta \pm \phi)$, is controlled by three parameters: the deposition angle θ, the pore width w, and the pore angle ϕ. θ (0° to 90°) is the angle at which the template is oriented towards the evaporation source and is, at the same time, the angle that the pore walls make with the vertical. The angle ϕ is the deviation of the pore from the normal plane of the template and is an artifact of the manufacturing process of the TEPC templates. The angle offsets, which vary from −34° to +34°, are largely responsible for the irregularities in the structures produced. Since the alignment of each individual pore can vary randomly from normal incidence in the template, no particular direction is favored in the template overall. TEPC templates are commercially available with smaller pore sizes (~10 nm–100 nm) and are utilized to fabricate nanowires.[27] Use of other templates may increase nanofingernail uniformity, such as anodized aluminum oxide (AAO). AAO is costlier, but the pores are periodic and close-packed and are known to be uniformly perpendicular to the template surface,[28] reducing the pore deviation. Overall, the smallest h is 0.1 μm and is achieved at θ = 75°, while the largest h is 2.6 μm and is achieved at θ = 30°.

Fig. 1 insets (i–iii) show the optical transmission 400–800 nm for 3 intermediate-h samples. The increased and broadened spectra, particularly with all-Au and Ag–Au samples are shown. The transmission is referenced to a glass substrate and unit-normalized to the maximum transmission. Compared with the corresponding micropore structures, enhanced optical transmission is observed near the multipolar plasmonic resonances (see also ESI†).

The I-GLAD structures are irregularly spaced on the substrate, depending on the height and angle of deposition, which is seen in the SEM images of Fig. 2. The percentage of nanofingernails to pores is smaller for taller nanofingernails, so that nanofingernails fabricated with lower deposition angle are more isolated. The all-gold nanofingernails exhibit a consistent transverse resonance at λ = 530 nm (light-blue line), whereas broader longitudinal resonances are present with shorter structures h < 0.2 μm. All-silver nanofingernails exhibit a consistent transverse resonance at λ = 380 nm (not shown); however, the longitudinal resonances are less marked in the transmission spectra.

The composite Au–Ag nanofingernails exhibit transmission spectra and resonant responses of both silver and gold; with both silver and gold, the nanofingernail structures achieve a plasmon response over a broader spectral range. With distinct silver and gold layers, a wider range of optical properties are available for sensing applications.[29] In order to determine the integrity of the gold and silver layers within the nanofingernail structure, a modified version of the I_2/KI etch process published by Microchemicals, Inc. is employed. An etch solution with a I_2 : KI : deionized water ratio of 0.25 g : 1 g : 40 mL is used, which results in an etch rate of 250 nm min^{-1}. Nanofingernail samples are exposed to the etching solution for 0, 5, and 10 s and subsequently characterized by SEM and energy dispersive spectroscopy (EDS).

The SEM images for the unetched and etched samples are shown in Fig. 3A, and the corresponding EDS analysis is shown in Fig. 3B. Prior to etching, the weight percentage ratio of Au to Ag is 3.86 [Fig. 3B(i)]. Exposure to the etching solution for 5 and 10 s reduces the weight percentage ratio to 2.03 and 0.14, respectively, as shown in Fig. 3B(ii–iii). The observation of compact nanofingernail structures in the SEM after the 10 s etch and the fact that the Au signal has been greatly diminished indicate that the nanofingernail structures are comprised of distinct gold and silver layers rather than a silver/gold alloy. This EDS analysis is valid across the entire sample, and indicates that even though the interface between the two metals maybe an amalgam of silver and gold, the outer nanofingernail layers exhibit integrity and are capable of carrying tunable and distinct plasmon resonances.

Analysis

Numerical simulations are first performed in order to understand the light interactions on an individual nanofingernail in the random array of nanofingernails, where the interactions

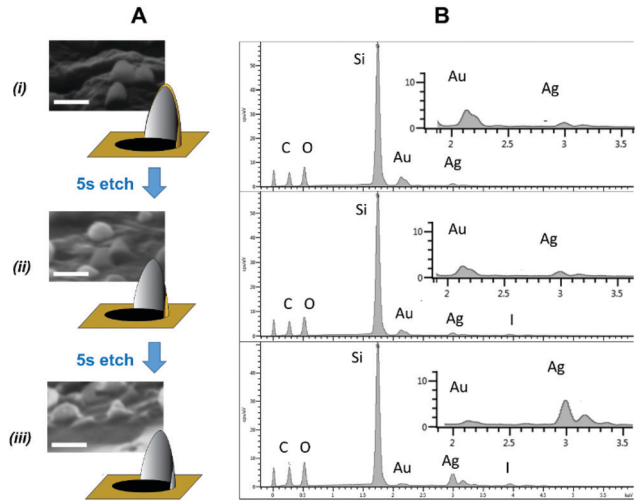

Fig. 3 (A) SEM images that show nanofingernails intact and (B) EDS spectra of nanofingernail samples (i) before iodide etch (ii) after a 5 s iodine etch (iii) after a 10 s iodine etch. Scale bars correspond to 2 μm. We note that as the gold layer is etched away (chemically confirmed by EDS), the silver layer remains intact and keeps its shape.

between nanofingernails are unimportant. Nanofingernails are modeled in a manner similar to ref. 30 with scattering boundary conditions. The optical response of the nanofingernail is modeled with the finite-element solver COMSOL. The illumination of circularly polarized light onto extrinsically-chiral out-of-plane nanofingernails results in intensity hotspots and near-field power flows that depend on the polarization helicity of light. A nanofingernail with an outer diameter of w = 1 μm in metal films of 100 nm thickness are illuminated with circularly polarized plane waves propagating in the –z direction.

Fig. 4(A–D) show the scattered fields surrounding a nanofingernail with h = 0.26 μm (θ = 75° for deposition), where circularly-polarized light with wavelength λ = 580 nm illuminates the nanofingernail. The scattered intensity profiles from round apertures are donut-shaped and carry phase singularities on the z-axis. The presence of the nanofingernail subsequently produces asymmetric donut intensity patterns [Fig. 4(A and B, i–ii)] and a complex, structured phase pattern. Even though the nanofingernails exhibit mirror symmetry across the y–z plane, the time-averaged scattered-field hotspots are not mirror images across the y–z plane [Fig. 4C]. The non-mirror symmetry field profiles from a mirror-symmetric nanostructure are a result of the interfering incident and scattered fields and the presence of the nanofingernail results in the scattered-fields being focused off-axis. The maximum amplitude of the scattered, longitudinal electric fields is 60% as large as the amplitude of the incident transverse fields. Peak values of the scattered hotspot fields with the nanofingernail are 30% larger than that of the scattered fields with aperture alone. This polarization-dependent enhancement of scattered fields of vertically-aligned nanostructures would increase detection sensitivity within the aperture.[31–33]

The scattered-field hotspots spiral along the propagation direction, where the direction of the hotspot rotation depends

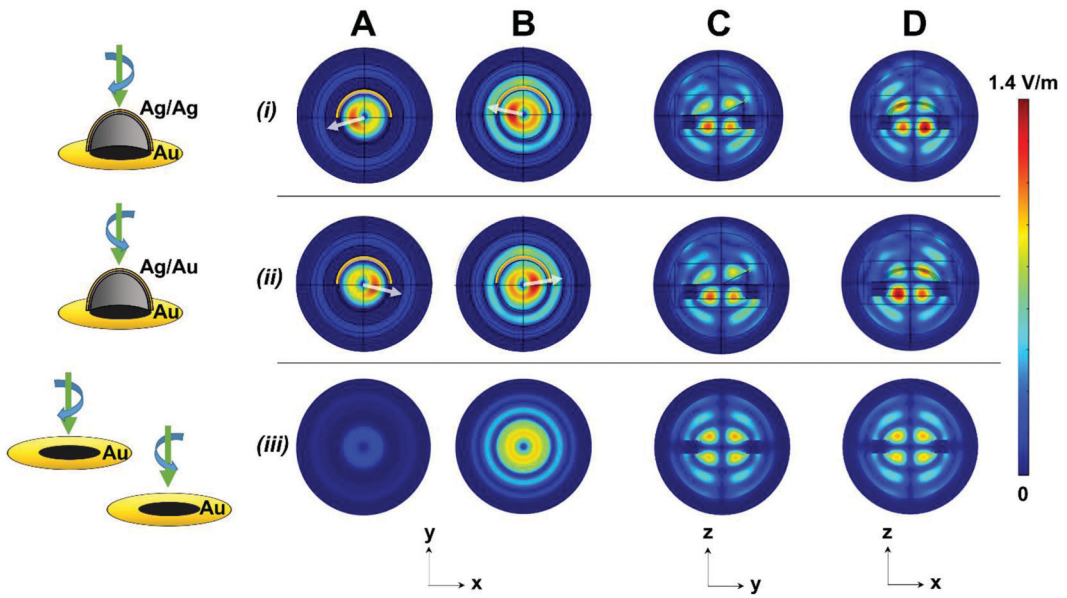

Fig. 4 Time-averaged magnitudes of the longitudinal (z-component) electric fields at λ = 580 nm (A) in the x–y plane in the center of the metal film and (B) in the x–y plane at the bottom plane of the metal film (C) in the y–z plane (D) in the x–z plane for (i) left-handed, (ii) right-handed circularly-polarized light on a nanofingernail (h = 0.26 μm) and aperture, and (iii) on an aperture alone. The white arrows show the direction of the scattered time-averaged hotspot, which spirals in the transverse plane as light propagates. Even though the nanofingernail structure exhibits mirror symmetry across the y–z plane, nanointerference between scattered and incident light leads to chiral time-averaged patterns that do not exhibit symmetry across the y–z plane.

on the handedness of incident light [Fig. 4(A and B,i–ii)]. In the x–y plane, C-shaped, broken-donut longitudinal magnetic-field profiles are present and rotate in the same direction as the scattered longitudinal fields [see ESI† for the magnetic-field simulations]. We emphasize that because the samples exhibit extrinsic chirality and mirror symmetry, that there is no circular dichroism observed. In other words, the enhanced chiral scattering is associated with a local superposition mode that is not observed in the far-field.

The chiral power flow arising from out-of-plane extrinsically-chiral structures is illustrated in the near-field hotspots [Fig. 5A]. A description of the whirlpool power flows[19,34] associated with the magnetic field is provided in the ESI.† Only a single image is necessary to show the intensity and power flow for both circular polarizations with aperture alone in the x–z and y–z planes, since these properties of the electromagnetic fields are identical for radially-symmetric structures. In contrast, three distinct images are necessary to illustrate the polarization-dependent behavior of the nanofingernail.

When illuminated at normal incidence, the presence of the nanofingernail refocuses the hotspots and shifts the location of the hotspot towards the illuminated substrate surface. For example, with λ = 580 nm, the light intensity is concentrated at the center plane of the 0.26 μm-tall aperture. However, with illumination in the presence of the nanofingernail, the light intensity is concentrated above the aperture, which raises the location of the hotspot approximately 150 nm. This feature of the raised hotspot, which occurs in a similar manner across the visible wavelength range, would enable detection of surface-adhered molecules more readily. When hotspots shift 150 nm towards the light source, the intensity increases 15%, which explains prior observations.[20]

Fig. 5B shows a projection of the curved, out-of-plane gold nanofingernail that is 200 nm thick and 260 nm tall; it lines the edge of a plasmonic aperture or nanopore with diameter of 1 μm. Chiral hybrid modes are observed between 400 and 800 nm for this structure and illustrated with the intensity colormaps. The oscillating intensity along the surface is a result of the simultaneous excitation of transverse and longitudinal modes. Colorplots of the curved nanofingernail surface show azimuthal standing modes along the curved edge of the nanofingernail. Line-outs of the time-averaged electric-field amplitudes in plane of mirror symmetry along the edge of the nanofingernail show longitudinal standing modes [Fig. 5C]. Azimuthal patterns flip across the plane of symmetry when illuminated with left-circularly polarized light (not shown).

Discussion and conclusion

The plasmonic modes supported by the nanofingernails under visible illumination in a periodic lattice explain the experi-

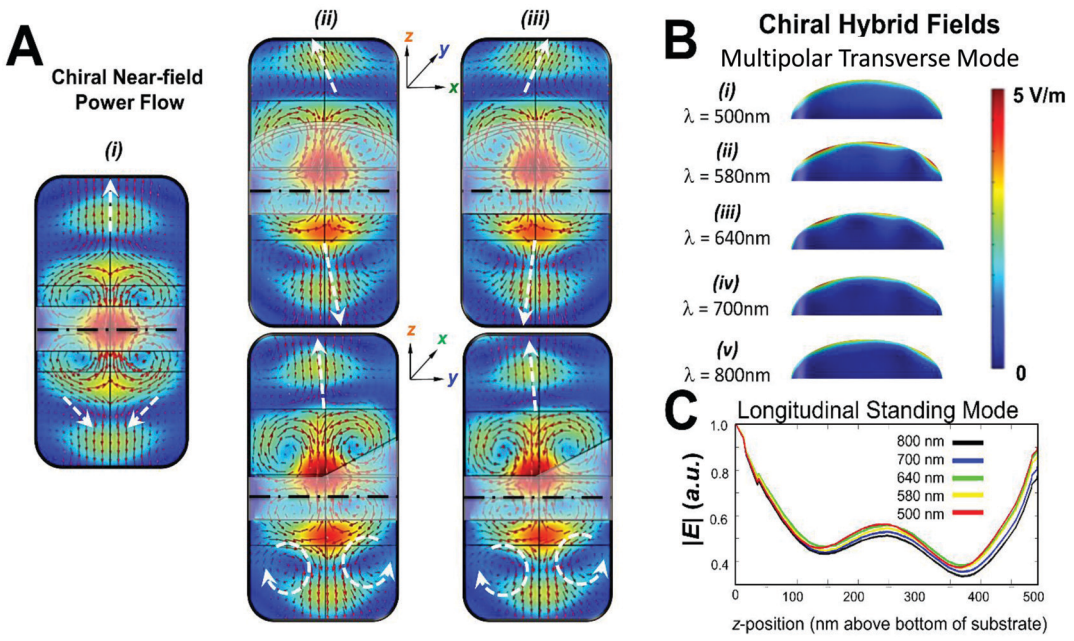

Fig. 5 (A) The symmetric intensity hotspots (colormap) and time-averaged power-flow vectors (arrows) around (i) a round aperture and chiral intensity hotspots and chiral power flow in the presence of a nanofingernail in the x–z plane (top) and in the y–z plane (bottom) for (ii) left-handed and (iii) right-handed circularly-polarized light. The center of the substrate metal (black dash-dot lines) provides a visual guide of the 150 nm vertical shift of the hotspot towards the incident light in the presence of the nanofingernail. The net power flow is angled away from the nanofingernail and the hotspots shift 150 nm towards the light source. Right-circularly polarized excitation at various visible wavelengths showing normalized time-averaged electric-field amplitudes of chiral hybrid modes. The wavelength is 640 nm. (B) Colorplots of the curved nanofingernail surface show azimuthal standing modes along the curved edge of the nanofingernail. Azimuthal patterns flip across y–z plane when illuminated with left-circularly polarized light (not shown). (C) Line-outs of the electric-field amplitudes in y–z plane at x = 0 show longitudinal standing modes.

mentally-measured and broadened optical transmission spectra of Fig. 1. The diameter of the holes under the nanofingernails is larger than the wavelength, approximately two to three times as large as the spectral interval of interest in this paper. Consequently, all of the modes excited on the nanofingernail substrates are multipolar modes, which are highly localized and very sensitive to the geometrical parameters. This is illustrated in Fig. 6 in a square lattice even though in experiments, the nanofingernails are present in a random array. Aperiodicity and irregularities of the nanofingernail—the result of statistical effects in the fabrication process, *e.g.*, nonuniform deposition and imperfect templates—and the aperiodic nature of the structures themselves, *e.g.*, variations in tilt, layer thickness, and height—lead to broadened features of the optical spectra. From Fig. 2, we see that taller nanofingernails have a higher tendency to be washed out in the fabrication process while the shorter nanofingernails persist through the fabrication process and are more closely spaced. The transmission spectra of tall nanofingernails resembles that of the micropores alone and isolated fingernail transmission. Pores without nanofingernails exhibit fewer inter-plasmon interactions and multipolar resonances than pores with nanofingernails. Shorter nanofingernails exhibit broadened multipolar plasmon resonances and enhanced interactions between nanofingernails. Additional discussion on the spectral features and nanofingernail modes is provided in the ESI.†

The presence of circular dichroism (CD) on an intrinsically-chiral structure is not necessary in order to achieve a chiral near-field response.[35] With nanofingernails, CD is achieved by tilting the nanofingernail arrays or illuminating the nanofingernails at oblique angles of incidence. CD measurements provided in the ESI† show that the nanofingernail substrates exhibit 2% CD when tilted 20-degrees but do not on average exhibit CD, as expected, when illuminated at normal incidence. Even when CD is not observed, the near-field hot spots spiral as a function of propagation close to the nanostructure.

Phase retardation effects are significant since the nanostructure dimension is larger than the wavelength.[36,37] One observation with the nanofingernail is that retardance, in the presence of hybrid modes with an obliquely-angled geometry, broadens the spatial hotspots and widens the spectral resonance. Also as a result of the retarded phase, we observe a "chirp" in the multipolar transverse mode. The degree of the chirp appears proportional to the absorption, which changes with nanofingernail curvature. This phase retardance associated with chiral hybrid modes may facilitate nonlinear optical interactions and favorable cascaded chemical reactions for these applications, where it is desirable that the areas of concentrated high intensity overlap spatially and overlap with different spectral wavelengths.[38]

Finally, since the presence of chiral hybrid modes on plasmonic nanowires has been associated with imbalanced and non-zero time-averaged Lorentz forces,[24] future applications of I-GLAD plasmonic structures in metal aperture arrays for sensing should consider the impact of the asymmetric, polarization-dependent plasmon-induced hotspots. Asymmetric intensity patterns are expected to yield asymmetric voltages or gradient or other dissipative dynamics arising from the excitation of chiral modes. As others have recently demonstrated a chiral force for enantiomeric separation of molecules with extrinsically-chiral plasmon structures,[39,40] the light interaction surrounding nanofingernails may selectively excite molecules flowing through the pore.

In conclusion, we illustrate the chiral multipole and enhanced plasmon near-field scattering that arises from out-of-plane, layered structures on the edges of apertures. An I-GLAD process produces out-of-plane, obliquely-cut, coaxially-layered nanoscale "nanofingernail" geometries around an aperture, enabling the optical excitation of the multipole plasmon modes. When illuminated at normal incidence, the presence of the nanofingernail refocuses the hotspots and shifts the location of the hotspot towards the illuminated substrate surface. The presence of the nanofingernail also results in polarization-dependent patterns of enhanced, near-field scattering, which indicates that nanofingernail structures made *via* I-GLAD would achieve higher detection sensitivities over broad-band illumination without a tilted substrate plane.[20] The combination of both spatial and spectral overlap

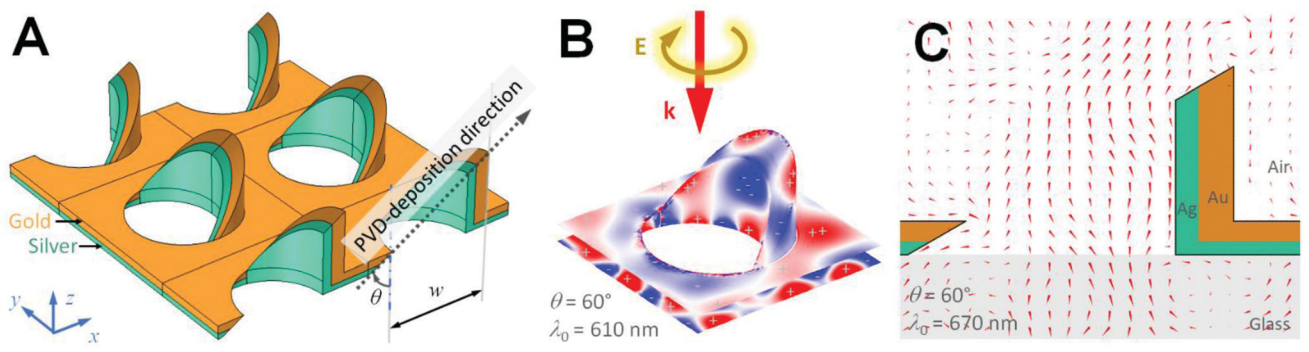

Fig. 6 (A) Geometry model of a nanofingernail array with gold and silver layers. The array period is 1.5 μm and deposition angle θ is 60° (B) Surface charge distribution at the metal surface under circularly polarized illumination at one of the calculated absorption maxima, showing strong multipolar plasmonic resonance. (C) Power flow (Poynting vector) in the x–z plane at one of the calculated transmission maxima. The lengths of the red arrows show the magnitude of the power flow in the logarithm scale.

of the near-field and chiral scattering is central to the design of nanostructures for nonlinear optical experiments. Such structures may be fabricated over large areas with I-GLAD.

Conflicts of interest

There are no conflicts to declare.

Acknowledgements

L. T. V. acknowledges funding from NSF DMR1921034 and NSF DMR 1151783. I. K. acknowledges partial support from the NSF-funded CREST IDEALS center (NSF HDR 1547830) as well as NSF CBET 1264550 and PSC CUNY Award 68871-00 46.

References

1 P. L. Stiles, J. A. Dieringer, N. C. Shah and R. P. V. Duyne, *Annu. Rev. Anal. Chem.*, 2008, **1**, 601–626.
2 J. R. Lakowicz, C. D. Geddes, I. Gryczynski, J. Malicka, Z. Gryczynski, K. Aslan, J. Lukomska, E. Matveeva, J. Zhang, R. Badugu and J. Huang, *J. Fluoresc.*, 2004, **14**, 425–441.
3 A. Kinkhabwala, Z. Yu, S. Fan, Y. Avlasevich, K. Müllen and W. E. Moerner, *Nat. Photonics*, 2009, **3**, 654–657.
4 A. G. Brolo, E. Arctander, R. Gordon, B. Leathem and K. L. Kavanagh, *Nano Lett.*, 2004, **4**, 2015–2018.
5 C. D. Kinz-Thompson, M. Palma, D. K. Pulukkunat, D. Chenet, J. Hone, S. J. Wind and R. L. Gonzalez, *ACS Nano*, 2013, **7**, 8158–8166.
6 M. P. Cecchini, A. Wiener, V. A. Turek, H. Chon, S. Lee, A. P. Ivanov, D. W. McComb, J. Choo, T. Albrecht, S. A. Maier and J. B. Edel, *Nano Lett.*, 2013, **13**, 4602–4609.
7 K. A. Willets, A. J. Wilson, V. Sundaresan and P. B. Joshi, *Chem. Rev.*, 2007, **117**, 7538–7582.
8 J.-R. Choi, K. Kim, Y. Oh, A. L. Kim, S. Y. Kim, J.-S. Shin and D. Kim, *Adv. Opt. Mater.*, 2014, **2**, 1–1.
9 X. Zhang, J. Jin, M. Pu, X. Li, X. Ma, P. Gao, Z. Zhao, Y. Wang, C. Wang and X. Luo, *Nanoscale*, 2017, **9**, 1409–1415.
10 Y. Pang and R. Gordon, Optical Trapping of a Single Protein, *Nano Lett.*, 2012, **12**, 402–406.
11 A. A. A. Balushi, A. Kotnala, S. Wheaton, R. M. Gelfand, Y. Rajashekara and R. Gordon, *Analyst*, 2015, **140**, 4760–4778.
12 H. Lee, C. Kim and D. Kim, *Sci. Rep.*, 2015, **5**, 17584.
13 N. Djaker, R. Hostein, E. Devaux, T. W. Ebbesen, H. Rigneault and J. Wenger, *J. Phys. Chem. C*, 2010, **114**, 16250–16256.
14 A. F. Coskun, A. E. Cetin, B. C. Galarreta, D. A. Alvarez, H. Altug and A. Ozcan, *Sci. Rep.*, 2014, **4**, 6789.
15 C. Escobedo, A. G. Brolo, R. Gordon and D. Sinton, *Nano Lett.*, 2012, **12**, 1592–1596.
16 Y. Y. Lee, R. M. Kim, S. W. Im, M. Balamurugan and K. T. Nam, *Nanoscale*, 2020, **12**, 58–66.
17 V. K. Valev, J. J. Baumberg, C. Sibilia and T. Verbiest, *Adv. Mater.*, 2013, **25**, 2517–2534.
18 E. Maguid, I. Yulevich, D. Veksler, V. Kleiner, M. L. Brongersma and E. Hasman, *Science*, 2016, **352**, 1202–1206.
19 K. Y. Bliokh, E. A. Ostrovskaya, M. A. Alonso, O. G. Rodrguez-Herrera, D. Lara and C. Dainty, *Opt. Express*, 2011, **19**, 26132.
20 W.-S. Tsai, K.-L. Lee, M.-Y. Pan and P.-K. Wei, *Opt. Lett.*, 2013, **38**, 4962.
21 J. S. Shumaker-Parry, H. Rochholz and M. Kreiter, *Adv. Mater.*, 2005, **17**, 2131–2134.
22 Y. Hou, H. M. Leung, C. T. Chan, J. Du, H. L.-W. Chan and D. Y. Lei, *Adv. Funct. Mater.*, 2016, **26**, 7807–7816.
23 Z. Wu, Y. Liu, E. H. Hill and Y. Zheng, *Nanoscale*, 2018, **10**, 18096–18112.
24 M. Moocarme, B. Kusin and L. T. Vuong, *Opt. Mater. Express*, 2014, **4**, 2355–2367.
25 S. Zhang, H. Wei, K. Bao, U. Håkanson, N. J. Halas, P. Nordlander and H. Xu, *Phys. Rev. Lett.*, 2011, **107**(9), 096801.
26 M. B. Cortie and A. M. McDonagh, *Chem. Rev.*, 2011, **111**, 3713–3735.
27 M. E. T. Molares, V. Buschmann, D. Dobrev, R. Neumann, R. Scholz, I. U. Schuchert and J. Vetter, *Adv. Mater.*, 2001, **13**(1), 62–65.
28 H. Masuda and K. Fukuda, *Science*, 1995, **268**(5216), 1466–1468.
29 E. Hamidi-Asl, F. Dardenne, S. Pilehvar, R. Blust and K. De Wael, *Chemosensors*, 2016, **4**(3), 16.
30 E. Hendry, T. Carpy, J. Johnston, M. Popland, R. V. Mikhaylovskiy, A. J. Lapthorn, S. M. Kelly, L. D. Barron, N. Gadegaard and M. Kadodwala, *Nat. Nanotechnol.*, 2010, **5**, 783–787.
31 Y. Zhang, A. Barhoumi, J. B. Lassiter and N. J. Halas, *Nano Lett.*, 2011, **11**, 1838–1844.
32 C. Charnay, A. Lee, S.-Q. Man, C. E. Moran, C. Radloff, R. K. Bradley and N. J. Halas, *J. Phys. Chem. B*, 2003, **107**, 7327–7333.
33 R. Verre, M. Svedendahl, N. O. Länk, Z. J. Yang, G. Zengin, T. J. Antosiewicz and M. Käll, *Nano Lett.*, 2015, **16**, 98–104.
34 M. V. Bashevoy, V. A. Fedotov and N. I. Zheludev, *Opt. Express*, 2005, **13**, 8372–8379.
35 M. H. Alizadeh and B. M. Reinhard, *ACS Photonics*, 2015, **2**, 361–368.
36 T. J. Davis, K. C. Vernon and D. E. Gómez, *Opt. Express*, 2009, **17**, 23655.
37 B. Sain, R. Kaner and Y. Prior, *Light: Sci. Appl.*, 2017, **6**, e17072–e17072.
38 G. D. Bernasconi, J. Butet and O. J. F. Martin, *J. Opt. Soc. Am. B*, 2016, **33**, 768–779.
39 T. Cao and Y. Qiu, *Nanoscale*, 2018, **10**, 566–574.
40 H. A. A. Champi, R. H. Bustamante and W. J. Salcedo, *Opt. Mater. Express*/, 2019, **9**, 1763.